RSC Advances

PAPER

View Article Online
View Journal | View Issue

Cite this: *RSC Adv.*, 2022, **12**, 4240

Advanced titanium dioxide fluidizable nanowire photocatalysts†

Kevin Reilly,[a] Babak Adeli,[a] Baizeng Fang,[a] David P. Wilkinson[ab] and Fariborz Taghipour*[ab]

In photocatalytic water splitting, fluidization is known to minimize the adverse effects of mass-transfer, poor radiation distribution, parasitic back-reactions and photocatalyst handling difficulties, which limit the scalability of immobilized-film and suspended slurry photocatalysts. Fluidization of one-dimensional TiO_2 photocatalyst particles, such as nanorods, -wires and -ribbons, is highly desired as it further enhances the efficiency of photocatalytic reaction, due to their peculiar photo-electrochemical characteristics that result in more effective separation of photo-generated charges and absorption of photons. However, the harsh physical environment of a fluidized bed reactor does not readily allow for nanostructured TiO_2 photocatalysts, as the fine features would be quickly removed from the particle surface. Here, we propose a scalable method for fabrication of rutile TiO_2 nanorods on porous glass beads as a 3D protective substrate to reduce the attrition rate caused by fluidization. The quality of the synthesized nanorod films was optimized through controlling a growth quality factor, R_q, allowing for good quality films to be grown in different batch amounts and different hydrothermal reactor sizes. The utilization of porous glass beads substrate has reduced the attrition rate, and the protective features of the particles reduced the rate of attrition by an order of magnitude, compared to a particulate photocatalyst, to near negligible levels. Such considerably reduced attrition makes the as-developed porous glass beads supported rutile TiO_2 nanorods a viable fluidizable photocatalyst candidate for various applications, including water splitting and degradation of organic compounds.

Received 17th October 2021
Accepted 4th January 2022

DOI: 10.1039/d1ra07681g

rsc.li/rsc-advances

1. Introduction

Growing global energy concerns and an increasing public environmental awareness have been fueling the adoption of clean energy technologies, particularly in the automotive and household power sectors, which has resulted in an increased demand for clean hydrogen fuels. Photocatalytic water splitting has long been sought after as an emissions-free, sustainable, direct solar-to-chemical energy conversion method to replace or augment current hydrogen production from conventional energy sources.

Titanium dioxide (TiO_2) has been one of the most extensively researched photocatalyst materials for both water splitting and water treatment[1] due to its low-cost, high stability and large band gap.[2–4] While excellent photocatalytic water splitting research has been carried out over several decades, there have been few reported attempts toward creating a scalable process. Our group has recently demonstrated that photocatalytic water splitting in a UV-irradiated fluidized bed reactor resulted in a marked increase in the efficiency of the process, while simultaneously minimizing mass-transfer effects, poor radiation distribution, parasitic back-reactions and photocatalyst handling difficulties which limit scalability of immobilized-film and suspended slurry photocatalysts.[5] The inherent nature of fluidized bed reactors also allows for relatively simple scaling of the process. Moreover, we have presented a model describing a fluidized water splitting reactor that provides further insight into the optimization and scaling of such systems.[5]

While the fluidization of TiO_2 photocatalysts yields excellent performance and a scalable process, the rigors of fluidization induce a great deal of mechanical stress, resulting in the rapid attrition of the particles, thus limiting the exploration of advanced photocatalyst designs. One-dimensional (1-D) TiO_2 photocatalyst particles, such as nanorods, -wires and -ribbons, are highly desired as they have demonstrated excellent performance for both water splitting[6–9] and photocatalytic water treatment[10–13] due, largely, to their excellent charge transport and separation properties. The highly ordered nanostructure of 1-D photocatalyst arrays greatly reduces the density of grain boundaries, which subsequently reduces the recombination of photogenerated electrons and holes,[14] and serves to reduce the

[a]Department of Chemical and Biological Engineering, University of British Columbia, 2360 East Mall, Vancouver, British Columbia V6T 1Z3, Canada. E-mail: fariborz.taghipour@ubc.ca

[b]Clean Energy Research Center (CERC), University of British Columbia, 2360 East Mall, Vancouver, British Columbia V6T 1Z3, Canada

† Electronic supplementary information (ESI) available. See DOI: 10.1039/d1ra07681g

reflection of incident light and improve the absorption of photons.[15] The harsh physical environment of a fluidized bed reactor does not readily allow for nanostructured TiO_2 photocatalysts, as the fine features would be quickly removed from the particle surface. Some researchers approached this obstacle by tailoring the mechanical characteristics of nanostructured TiO_2 throughout the synthesis.[16] Several researchers have successfully deposited TiO_2 photocatalysts onto porous, fluidizable particles to protect photocatalyst coatings from particle-to-particle and particle-to-wall collisions, which greatly reduced the mechanical ablation of the photocatalyst layer.[17–20] The research group of Langford and Kantzas[18–22] has aptly described the structure of the porous support particles as being "golf ball"-like, wherein the rough surface of the particles created many indentations (much like the "dimples" of a golf ball) in which the deposited TiO_2 photocatalyst coating could reside and remain protected from mechanical ablation during fluidization. Such porous, "golf ball"-like particles may provide sufficient protection to allow the use of 1-D nanostructured films on their surface.

One-dimensional nanostructured TiO_2 films have been synthesized *via* a number of methods,[12,23,24] however, hydrothermal growth has proven to be of the most facile and popular methods.[25–35] Recent studies have investigated the synthetic parameters in hydrothermal growth of nanostructured TiO_2 films in detail.[36,37] The hydrothermal growth method presented by Liu and Aydil[38] has become one of the most popular and highly cited methods due to its relative simplicity. This method, however, results in nanorods with the rutile crystalline structure, which typically has been shown to be less active than anatase TiO_2, particularly for energy conversion applications.[6,39–45] The solution-based hydrothermal nanorod growth method, however, allows for all surfaces of the porous particles to be deposited with nanorods and nanowires in a single processing step and enables more control over the characteristics and morphology of the synthesized photocatalyst.[46–48] In spite of its great potential, only a few examples of hydrothermal growth of TiO_2 nanorods and nanowires on porous or high surface-area substrates have been published.[11,49,50] Furthermore, there has not been any work, to our knowledge, describing the scale-up of a hydrothermal method to allow for the large-scale synthesis of TiO_2 nanorods immobilized on porous substrate.

Several researchers and ourselves have presented several low-temperature chemical bath deposition (CBD) techniques that allow for long titanate nanowires to be deposited easy on a wide variety of substrates;[11,51] these titanate nanowires are then converted to anatase TiO_2 nanowires by calcination or crystallization in acidic hydrothermal baths.[11,52,53] It is worth noting that calcination plays an important role in the photocatalytic activity of the fabricated TiO_2 nanowires.[54] As these low-temperature methods do not require specialized reaction vessels like the hydrothermal methods, they offer a greater degree of flexibility when attempting to scale the production of nanowire deposited substrates.

This article, to our knowledge, presents for the first time the scalable fabrication of TiO_2 rutile nanorods and anatase nanowires photocatalysts on porous, fluidizable substrates for use in a UV-irradiated fluidized bed reactor. Moreover, we present two methods that expand upon both our own CBD nanowire process and the popular hydrothermal nanorod method to allow for scalable production of fluidizable nanorod photocatalysts, in which addresses the main obstacle of conventional slurry-based and thin-film based photocatalytic systems, including the attrition and limited mass transfer, respectively. In this work, nanowire refers to the high aspect ratio (*i.e.*, long and thin) 1-D anatase TiO_2 structures produced *via* CBD whereas nanorod refers to the low aspect ratio (*i.e.* short and broad) 1-D rutile TiO_2 structures produced *via* the hydrothermal growth method. Further, a framework for tailoring the dimensions of the synthesized TiO_2 nanowires, on a porous substrate, is proposed. The methodology presented here offers a powerful framework for designing and fabrication of highly efficient photocatalytic fluidized bed systems with enhanced quantum efficiencies, owing to their superior photon absorption, improved charge carriers separation, enhanced rate of mass transfer, and nearly negligible rate of particle–particle attrition.

2. Experimental

2.1. Materials

Porous glass beads (Siran™ #4711, 1–2 mm diameter, Jaeger Biotech), as shown in Fig. S1 (ESI†), were employed as porous substrates for the synthesis of the fluidizable nanowire/nanorod-deposited particles. The porous particles were measured to have a dry bulk density of 568 kg m^{-3} and a mean diameter of 1.6 mm. The manufacturer-supplied specifications report the pore diameters <120 μm, pore volume to be 55–60% and surface area as 87 056 m^2 m^{-3} (*i.e.*, ~1.53 m^2 g^{-1}).

Before use, the as-received porous glass beads were first cleaned by ultrasonication in a 1 : 1 : 1 mixture of acetone, isopropyl alcohol, and deionized water for 30 minutes, followed by ultrasonication in deionized water for 30 minutes. The particles were then drained and dried in an oven at 80 °C.

2.2. Synthesis of anatase nanowire-coated particles

The porous glass beads were first deposited with a TiO_2 seed layer by placing 20 g of the bare substrate into 80 mL of a 0.2 M aqueous $TiCl_4$ solution. The porous beads were allowed to soak in the solution for 12 hours, then rinsed with deionized water to remove excess solution and dried at 80 °C. The TiO_2 seed-deposited beads were then calcined in air at 450 °C for 1 hour in an oven.

A growth solution was prepared by mixing 800 mL of 30 wt% hydrogen peroxide (H_2O_2, Fisher) and 24 mL of nitric acid (HNO_3, Fisher) for 10 minutes, followed by 2.4 g of potassium titanium oxalate (PTO, Sigma Aldrich) and 1.6 g of melamine (Sigma Aldrich). The solution was gently heated to 40 °C while stirring stirred to aid the complete dissolution of melamine, yielding an intense red-orange PTO-H_2O_2 solution. The solution was then transferred to a 1 liter glass vessel containing 0–40 g of the seed-deposited porous beads. The glass vessel was sealed loosely to minimize evaporation while avoiding pressurization of the vessel by gases evolved during nanowire growth, and then

placed in an oven at 80 °C for 7 hours. The titanate nanowire-deposited beads were first rinsed with deionized water, and then placed in a 1 M HCl solution for 15 minutes. The particles were then decanted from the solutions and rinsed thoroughly with deionized water until the wash water measured a pH of 6–7; the particles were then dried at 80 °C in an oven. The titanate nanowires were converted to anatase TiO_2 nanowires by calcining the nanowire-deposited beads in air at 550 °C for 1 hour in a furnace.

2.3. Synthesis of rutile nanorod-coated particles

It was observed that highly acid hydrothermal conditions occasionally resulted in the dissolution of the TiO_2 seed layer formed by the $TiCl_4$ treatment described above, resulting in delamination of the nanorod layer, therefor an alternative seed layer method was developed based on a TiO_2/sol–gel composite method described by Keshmiri *et al.*[55] A solution containing 17.6 mL of ethanol, 1.2 mL of H_2O and 2.9 mL of HCl was mixed in a beaker for 10 minutes. Titanium tetraisopropoxide (TTIP, 22 mL, Sigma Aldrich) was added drop-wise to the solution while stirring and allowed to mix for 1 h. Commercial TiO_2 powder (7 g, Evonik P25) was added to the solution and left to stir overnight. The solution was then diluted with 81.3 mL of ethanol and allowed to mix for 1 hour. The composite solution was transferred to a 250 mL beaker. Porous glass beads (100 g) were placed in a stainless steel mesh basket and immersed in the composite solution and allowed to soak for 10 minutes; the beads were stirred occasionally with a glass rod to dislodge any air bubbles trapped on the surface of the beads. The basket was then withdrawn from the solution slowly, allowing excess solution to drain away. The coated beads were spread on a tray in a single layer and allowed to dry at room temperature overnight. The beads were then calcined at 500 °C for 1 hour. This process was repeated twice to achieve a strong and uniform TiO_2 layer over the entire particle surface.

In a large beaker, 50–150 mL of deionized water and 50–150 mL of concentrated hydrochloric acid were mixed to yield a total volume of 200 mL. TTIP was added to the solution in varying amounts (0–20 mL) and mixed for 10 minutes. The solution was then transferred to a 500 mL Teflon-lined hydrothermal vessel containing 0–20 g of the TiO_2-composite coated porous beads. The sealed vessel was placed in an oven at 150 °C for up to 18 hours. The vessel was then cooled under running water to room temperature. The growth solution was carefully decanted from the vessel and the nanorod-coated beads were recovered in a fine mesh basket. The beads were then gently washed with in a 50 : 50 water/HCl bath to remove excess solution (while avoiding hydrolysis), followed by gentle rinsing with deionized water until the wash water measured a pH of 6–7. The nanorod-coated beads were dried in an oven at 80 °C overnight, followed by calcining in an oven at 550 °C for 1 hour.

2.4. Configuration of UV-irradiated fluidized bed reactor system

The UV-irradiated fluidized bed system and its operation has been described in detail in our previous study.[5] In brief, an annular fluidized bed, with a quartz glass tube inner annulus, containing a low-pressure mercury vapor ultraviolet (UV) lamp (Emperor Aquatics, 50 W, 254 nm), and a polycarbonate outer annulus, was employed. The UV lamp was not employed in this study. The photocatalytic reaction zone between the quartz glass tube and the outer polycarbonate wall has an inner radius of 1.41 cm, an outer radius of 2.54 cm and an effective length of 32.76 cm, yielding a total fluidized reactor volume of 0.45 L. The inlet of the fluidized bed reactor was comprised of a conical flow distributor designed to avoid jetting. The outlet ports of the fluidized bed reactor were connected directly to a separator unit having a volume of 0.40 L. The reaction solution was circulated from the separator back to the fluidized bed reactor inlet by a PanWorld NH-100PX centrifugal pump. A stainless-steel mesh filter was placed over the outlet of the separator to avoid entrainment of any eluted particles into the pump (where they would be macerated by the impeller). A National Instruments USB-6212 Data Acquisition (DAQ) card was used to provide direct control of the UV lamp and centrifugal circulation pump.

2.5. Measurements of attrition resistance

The rate of attrition was determined using a spectrophotometric technique.[56] Briefly, 70 mL of photocatalyst particles are loaded into the fluidized bed reactor system, which was then filled with 1 L of deionized water. The photocatalyst particles were then fluidized to an expanded bed height of 24 cm and 10 mL of samples of the liquid phase were taken at several intervals. The UV lamp was not employed during the attrition tests.

A solution (Solution A) was prepared by dissolving $(NH_4)_2SO_4$ (3 M) in concentrated H_2SO_4. Solution B consisted of a 1.8 M aqueous H_2SO_4 solution. The 10 mL of aliquots containing TiO_2 were transferred to a ceramic dish, to which was then added 10 mL of Solution A. The mixture was then heated over a Bunsen burner until boiling and the TiO_2 dissolved (~10–20 minutes). The mixture was then qualitatively transferred to a 25 mL volumetric flask using 5 mL deionized water. The volumetric flask was then filled to 25 mL with Solution B, then 200 μL of H_2O_2 was added. The flask was then inverted and agitated to form a yellow-orange peroxo–titanium complex. The concentration of Ti^{4+} was then measured using a Cary 100 photospectrometer by measuring the absorbance at 410 nm.

2.6. Characterization

The particles were characterized by X-ray diffraction (XRD) using a Bruker D2 Phaser desktop X-ray diffractometer using Cu-Kα radiation (1.5418 Å). As the nanowire/-rod surface layer on the porous glass particles was minute compared to the total bulk of the particles, it was often not possible to detect the peaks arising from the 1-D nanoparticles once the nanowire/-rod deposited glass particles were finely ground and prepared for analysis. An alternate method was devised and a custom sample holder that could hold a sufficient depth of whole particles was produced. Whole particles were then loaded into the sample holder and leveled as flat as possible. The loaded sample holder was placed into the diffractometer and XRD

measurements were then made while rotating the sample holder at a speed of 2 rpm. This approach averaged irregularities in the sample surface exposed to the detector and produced diffractograms displaying peaks that indexed well with diffractograms of the 1-D nanoparticles grown on flat indium–tin oxide (ITO) coated glass slides. It should be noted that while this method was sufficient to identify the TiO_2 phases present on the porous glass particle surface, the results may be inadequate for further analyses requiring peak intensities (*i.e.* elemental and phase composition).

SEM imaging and energy-dispersive X-ray spectroscopy (EDX) were conducted on both the Hitachi S-2600N Variable Pressure Scanning Electron Microscope (VPSEM) and the Hitachi S3000N VP-SEM with EDX. The samples were mounted on adhesive carbon tape and coated with a 5 nm platinum layer. Imaging was carried out at 5 kV to avoid electrostatic distortion of the images due to charging of the TiO_2 and glass particles. Transmission Electron Microscopy (TEM) imaging was conducted on a FEI Tecnai G2 200 kV Transmission Electron Microscope. The nanowire and nanorod rod deposited particles were ground in an agate mortar, then sonicated in pure ethanol. The fine TiO_2 particles dispersed in ethanol were then dropped on to TEM grids and allowed to dry at 80 °C for 5 hours before imaging. ImageJ software was used to manually measure the nanowire and nanorod dimensions from the SEM and TEM images, as well as to determine the crystal lattice interlayer distances by Fast Fourier Transform (FFT) analysis of the TEM images. UV-Vis Diffuse Reflectance (UV-Vis-DR) spectra of the deposited films were measured by using an Ocean Optics Flame UV spectrometer with a tungsten-deuterium light source (DH-2000-BAL) and reflectance probe.

3. Results and discussion

Scalable fabrication of TiO_2 rutile nanorods and anatase nanowires photocatalysts on porous, fluidizable substrates was investigated through two developed synthesis routes, the chemical bath deposition and modified hydrothermal growth. Accordingly, the structural, elemental, and optical characteristics of the synthesized nanostructures, as well as the effect of fabrication conditions were studied in detail. The obtained information was utilized to optimize the growth mechanism and control the morphology and crystallography of the synthesized fluidizable photocatalyst towards enhanced quantum efficiencies and durability of photocatalytic system.

3.1. Anatase nanowire growth

Titanate nanowires were grown on the porous $TiCl_4$-seeded particles *via* a low-temperature chemical bath deposition (CBD) method. Unlike the hydrothermal growth method, the CBD process does not require a specialized reaction vessel, thus the reactor vessel size could be readily varied to produce desired batch sizes. As this method employs the use of a water-soluble peroxo–titanium complex, the initial $[Ti^{4+}]$ concentration could be varied; however, $[Ti^{4+}]$ was held constant at 8 mM for these experiments.

While titanate nanowires could be grown on the same TiO_2-composite seeded particles employed for the hydrothermally grown samples, it was found that the presence of the thick TiO_2 seed layer catalyzed the decomposition of H_2O_2. This in turn led to a rapid evolution of gas, making the reaction violent; this was especially prevalent for high $[M_{cat}]/[V_{sol}]$ ratios, where M_{cat} and V_{sol} are the mass of seed particles and the growth solution volume, respectively. The use of $TiCl_4$-seeded porous particles resulted in a reduced rate of gas evolution and a gentler nanowire growth phase. As such, the $TiCl_4$-seeded particles were preferred from a safety and practicality standpoint. It was observed that the gas bubbles evolved during nanowire growth caused the porous particles to fluidize and tumble in the reaction vessel. In contrast to the hydrothermal growth of nanorods, where the particles form a packed bed, it is believed that this mixing resulted in improved nanowire growth and particle-to-particle consistency, as well as served to minimize the accumulation of nanoparticles precipitated in solution (through homogeneous nucleation) on the particles surface.

It is well-established that the morphology, crystallography, optical characteristics, and chemistry of Titanate nanowires can be carefully tailored through synthesis parameter.[36,54,57] Titanate nanowires were grown on the porous seeded particles at $[M_{cat}]/[V_{sol}]$ ratios of 5×10^{-4}, 2.5×10^{-3}, 5×10^{-3}, 0.025 and 0.05 g mL^{-1} in an oven at 80 °C for 7 hours. The nanowire-deposited particles were then calcined at 550 °C for 1 hour to convert the titanate nanowires to anatase. For all $[M_{cat}]/[V_{sol}]$ ratios, dense films of vertically aligned nanowires were observed covering all surfaces of the porous particles (Fig. 1). In Fig. 1, it can be seen that for low $[M_{cat}]/[V_{sol}]$ ratios (*e.g.* $[M_{cat}]/[V_{sol}] = 5 \times 10^{-4}$), the surface of the particles are covered with flower-like nanowire "balls", which are the result of homogeneous nucleation, growth and precipitation of nanowires in solution. As the $[M_{cat}]/[V_{sol}]$ ratio increases, the quantity of nanoflower balls decreases and are largely absent for samples grown at $[M_{cat}]/[V_{sol}]$ ratios of 0.025 g mL^{-1} and 0.05 g mL^{-1}. This observation indicates that increasing the total surface area on which nanowires can grow promotes heterogeneous nucleation and reduces homogeneous nucleation in solution.

In Fig. 1k and n, regions of flattened nanowires can be seen on the apex points of the particle surface that are the result of the vigorous tumbling during nanowire growth and subsequent handling. Meanwhile, the majority of the nanowires (which reside in recesses below the apex points) remain intact; this demonstrates the effectiveness of the porous particle shape in protecting the nanowires during fluidization and from other mechanical damage.

As seen in Fig. 2a $[M_{cat}]/[V_{sol}]$ ratio of 5×10^{-4} g mL^{-1} yielded 2.42 μm long, 70 nm wide nanowires as a result of rapid nanowire growth. Increasing the ratio to 2.5×10^{-3} g mL^{-1} resulted in a sharp drop in both the nanowire diameter and length. From 2.5×10^{-3} g mL^{-1} to 0.025 g mL^{-1} the nanowire length decreased slightly while the diameter remained largely unchanged. Further increasing the $[M_{cat}]/[V_{sol}]$ ratio to 0.05 g mL^{-1}, however, resulted in the nanowire length deceasing sharply to 0.8 μm. The ideal $[M_{cat}]/[V_{sol}]$ ratio was thus chosen to be 0.025 g mL^{-1} to minimize the presence of nanowire balls

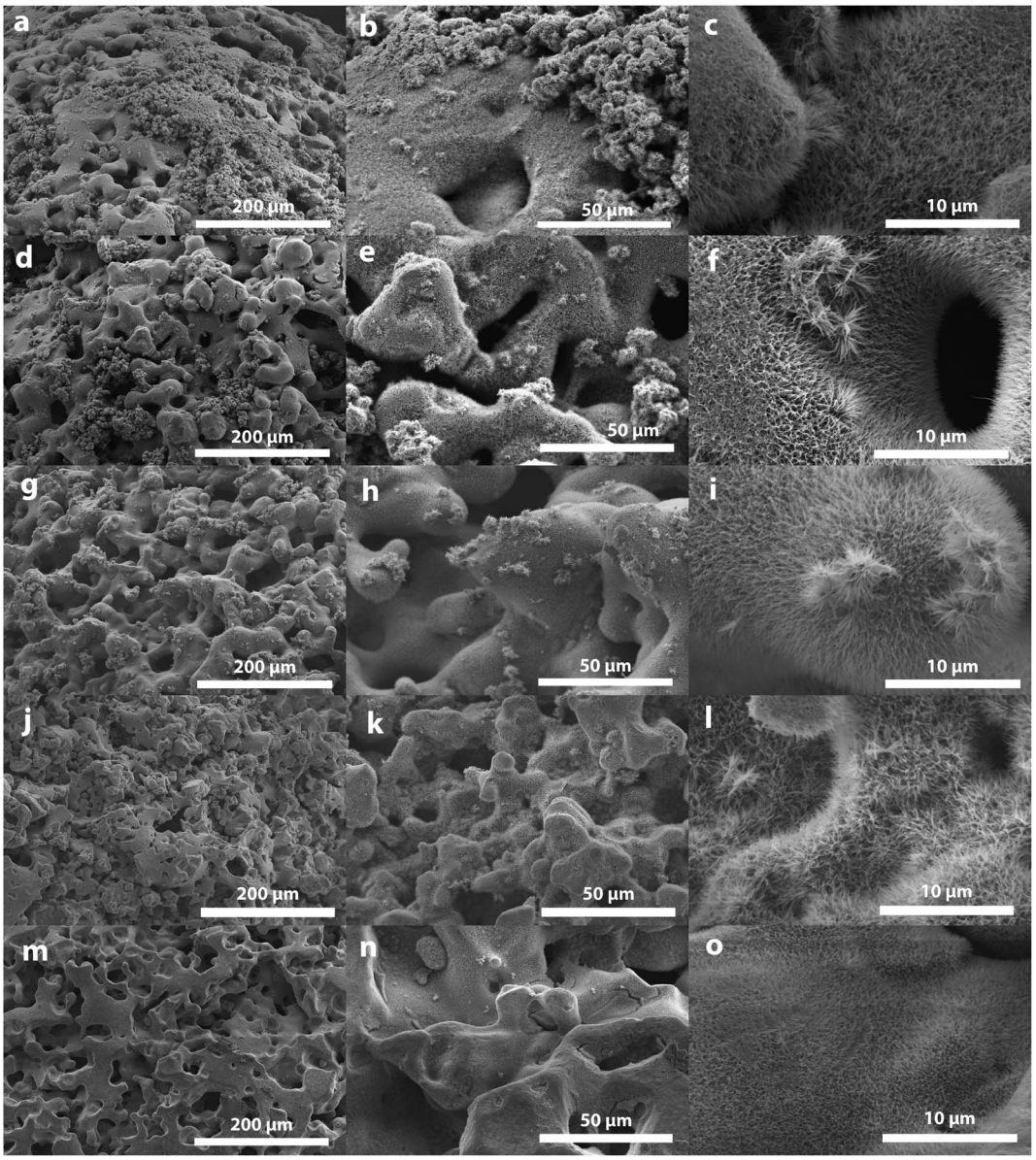

Fig. 1 SEM images of nanowire-deposited deposited particles grown at $[M_{cat}]/[V_{sol}]$ ratios of (a–c) 5×10^{-4}, (d–f) 2.5×10^{-3}, (g–i) 5×10^{-3}, (j–l) 0.025 and (m–o) 0.05 g mL^{-1}. M_{cat} and V_{sol} are the mass of seed particles and the growth solution volume.

(which may be easily ablated from the particle surface during fluidization) while maximizing the nanowire aspect ratio and maximizing the amount of nanowire-deposited photocatalyst particles that can be produced in a given batch.

3.2. Rutile nanorod growth

Rutile TiO_2 nanorods were grown on the TiO_2-composite coated porous glass particles using a modified hydrothermal vessel (HTV) growth method based on that originally presented by Liu and Aydil. Early attempts to scale the hydrothermal process to grow nanorods on porous particles in any substantial amount resulted in sporadic, inconsistent growth with high particle-to-particle variability where some particles were covered entirely with nanorods while others were completely devoid of nanorod growth. It was observed that particles at the top of the bed had better nanorod growth with those at the bottom typically had poor or no growth. Moreover, it was observed that, under certain conditions, the nanorods would delaminate or slough off the particle surface in sheets. Liu and Aydil observed a similar delamination issue for treatment times beyond 24 hours, where it was hypothesized that when the system reached an equilibrium between dissolution and growth processes (due to decreasing $[Ti^{4+}]$), dissolution at the glass/TiO_2 interface resulted in delamination of the deposited nanorod layer. We observed that the $TiCl_4$-treated particles were particularly prone to delamination, especially at high acid concentrations or high $[M_{cat}]/[V_{sol}]$ ratios. By employing the TiO_2-composite seed layer, which has been shown to be mechanically strong,[55,58] this delamination effect could be minimized.

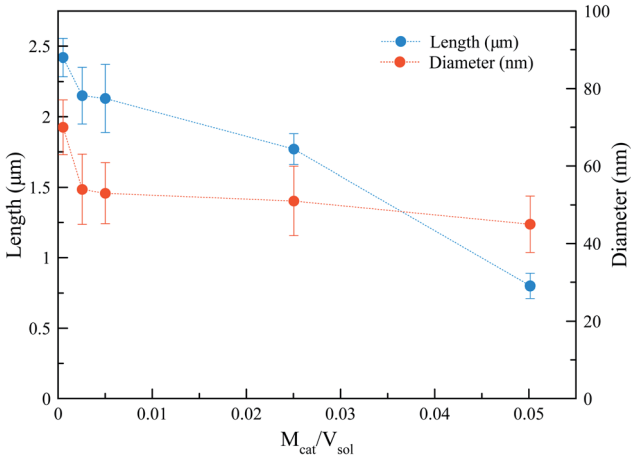

Fig. 2 Nanowire length and diameter dependence on $[M_{cat}]/[V_{sol}]$. M_{cat} and V_{sol} are the mass of seed particles and the growth solution volume.

The HCl/H_2O ratio, the amount of TTIP and the amount of porous substrate employed in the hydrothermal vessel were varied to determine conditions under which nanorods could be successfully grown on significant amounts of the porous particles. The various trials are summarized in Table S1 (ESI†). While the dimensions of the resulting nanorods could be easily described quantitatively, the extent of surface coverage, the nanorod film quality and the particle-to-particle variability could only be described in qualitative terms. The quality of the resulting nanorod-deposited particles was roughly classified into the following three categories: (1) Class I (good), in which dense, vertically aligned nanorod were grown on all sampled particles with little particle-to-particle variability. In addition, there were only few, if any, regions devoid of nanorods, and no delamination of the nanorod films; (2) Class II (moderate), in which nanorod were grown on all sampled particles with some variability in nanorod density across particle surface. There was little particle-to-particle variability. In addition, there were only few bare regions or regions with low nanorod density, and no delamination of the nanorod films; and (3) Class III (poor), in which patchy, sporadic or no nanorod were grown on the substrate, there was a moderate to high particle-to-particle variability, and also significant delamination of the nanorod films.

Some examples of Class I (good), Class II (moderate) and Class III (poor) quality nanorod films are shown in Fig. 3a, b, and c, respectively.

It was found that this classification followed a trend with a ratio, R_q, which was defined as:

$$R_q = \frac{[H^+]M_{cat}}{[TTIP]V_{sol}} \quad (1)$$

where $[H^+]$ and [TTIP] are the initial H^+ and TTIP concentrations (mol L^{-1}), while M_{cat} and V_{sol} are the mass of porous particles and the total solution volume employed in the HTVs. A clear trend in the quality of the nanorod-deposited particles can be seen in Fig. 4, where R_q was plotted *versus* $[H^+]/[TTIP]$ for each trial and the markers were labeled according to the corresponding classification. It was observed that for constant (V_{sol}/M_{cat}) (corresponding to the slope of the diagonal lines) that the quality of the particles increases with decreasing R_q (Class I). This may be viewed either as the particle quality increasing with lower $[H^+]/[TTIP]$ ratios, where higher [TTIP] results in higher rate nanorod nucleation and growth, or increasing with lower $M_{cat}/([TTIP]V_{sol})$ ratios, where a minimum total number of moles of TTIP is required for proper nanorod growth. Similarly,

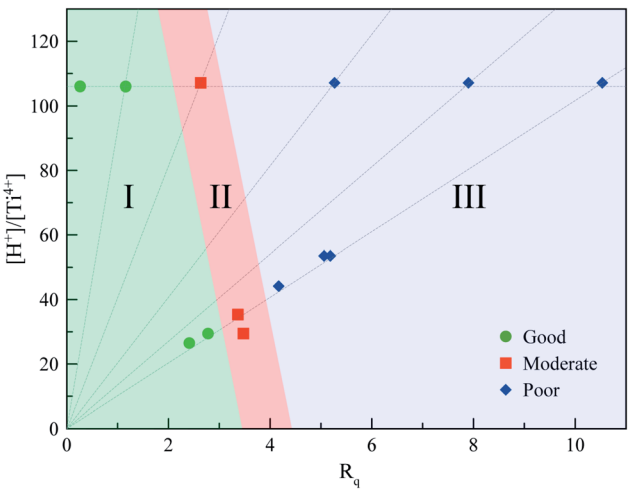

Fig. 4 Nanorod film quality classification *versus* R_q. The ratio R_q defined as $[H^+]M_{cat}/[TTIP]V_{sol}$ where $[H^+]$ and [TTIP] are the initial H^+ and TTIP concentrations (mol L^{-1}), while M_{cat} and V_{sol} are the mass of porous particles and the total solution volume employed in the HTVs.

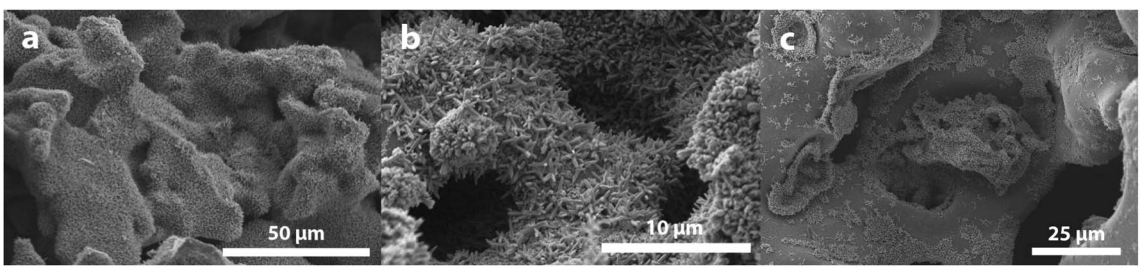

Fig. 3 Examples of the quality of the resulting nanorod-deposited particles films exhibiting (a) Class I (good), (b) Class II (moderate) and (c) Class III (poor) quality.

for constant $[H^+]/[TTIP]$, corresponding to the horizontal lines in Fig. 4, the quality of the particles increases with decreasing Rq, implying an ideal $[M_{cat}]/[V_{sol}]$ ratio. The range of R_q values defining the Class II (moderate) region were not constant but rather appear to have a dependence on the $[H^+]/[TTIP]$ ratio, however, it was not possible to derive an explanation for this relationship. The observed relationship between R_q and the particle quality could be reliably reproduced in a smaller 180 mL hydrothermal vessel, indicating that the relationship is independent of the vessel size (at least for vessels less than 500 mL). It should be noted that the same fill percentage, $V_{sol}/V_{reactor}$, was employed for both vessels.

No clear relationship between R_q and the nanorod dimensions could be observed; however, it was noted that for solutions employing 1 : 1 volume ratios of HCl/H_2O, the nanorods typically grew to lengths between 1.1 and 1.4 μm. It was simultaneously observed that in 1 : 1 HCl/H_2O solutions, the amount of TTIP could not be easily increased beyond 12 mL of (0.187 mol L^{-1}) without the formation of significant amounts of precipitate, both during preparation of the growth solution and during nanorod growth in the hydrothermal vessel. It is hypothesized that the high H_2O content of these solutions leads to rapid hydrolysis of the TTIP, especially so as the TTIP concentration increases, which results in the homogeneous nucleation and precipitation of TiO_2 in solution. This homogeneous nucleation and precipitation compete with the heterogeneous nucleation and growth of nanorods, resulting in shortened nanorod lengths.

It was found that by increasing the HCl/H_2O ratio to 3 : 1, the amount of TTIP could be increased to 20 mL (0.3 mol L^{-1}) without the formation of precipitate, which in turn resulted in a ~200% increase in the nanorod length to 2.8 μm. It should be noted, however, that by increasing the HCl/H_2O ratio to 3 : 1, the minimum amount of TTIP is required to achieve nanorod growth increases (as R_q increases); indeed, it was observed that for a 3 : 1 HCl/H_2O solution, 12 mL (0.187 mol L^{-1}) of TTIP resulted in little-to-no nanorod growth. It is hypothesized that the increased $[H^+]$ and reduced H_2O content of these solutions slows the rate of hydrolysis, reduces homogeneous nucleation and allows for a greater amount of TTIP to be dissolved in solution, the combination of which resulting in the growth of longer nanowires; however, the high $[H^+]$ may result in the inhibition of nanorod growth entirely if [TTIP] is not sufficiently high. It was noted that increasing the HCl/H_2O ratio resulted in a notable change of the nanorod shape; nanorods grown at lower HCl/H_2O ratios typically had straight sides and square ends, whereas nanorods formed in high HCl/H_2O ratio solutions had a pronounced tapered shape (Fig. 5). This may be a result of the higher $[H^+]$ having a more pronounced effect on growth rate where, as the concentration of Ti in solution decreases during the course of nanorod growth, the rate of growth will reduce more sharply than solutions with lower H^+ concentrations, resulting in the tapered shape.

For nearly all growth conditions, the nanorods were observed to consist of bundles of smaller diameter nanorods. It was found that the addition of KCl (up to 12 g) lead to a slight reduction in both the average diameter of the bundles and the smaller nanorods that comprise them. A similar effect has been reported where the addition of NaCl led to reduced nanorod diameters;[38,59] this effect was discussed to be due to selective adsorption of Cl^- on certain facets or due to electrostatic screening. The relative increase in $[Cl^-]$ due to the addition of KCl, however, is small, as will be any increase in Cl^- adsorption, thus is it suspected that the reduction in nanorod diameter was due primarily to the latter effect.

It was observed that the addition of KCl resulted in an increase of an immiscible organic phase suspended on top of the growth solution; this immiscible phase is presumed to be an isopropoxide species resulting from the hydrolysis of TTIP. It was necessary to carefully decant the immiscible organic layer before removing the particles from the HTV as the organic layer would easily contaminate the surface of the nanorod-deposited particles and impart a hydrophobic behavior after drying and calcination. Calcining organic-contaminated particles in air resulted in the formation of a graphite-like layer on the surface of the nanorods. TEM imaging (Fig. 6) shows that the graphitic layer was 1.5 nm thick. The interplanar spacing of the graphitic layer was 3.3 Å, which is in agreement with (002) *d*-spacing values reported in literature.[60–62] The ideal hydrothermal growth conditions were chosen to be those corresponding with HTV-18 (Table S1†) as these conditions yielded dense growth of 2.8 μm nanorods over the entire particle surface. Moreover, KCl was not added to the solution to over exacerbation of the organic phase to avoid contamination of the particle surface.

3.3. Characterization

Titanate nanowires were grown on the porous, seeded particles at a $[M_{cat}]/[V_{sol}]$ ratio of 0.025 g mL^{-1} in an oven at 80 °C for 7 hours, then calcined at 550 °C in air for 1 hour to convert the titanate nanowires to anatase. XRD analysis of the calcined particles (a) revealed the nanowires to be anatase (JCPDS 00-021-1272) with the addition of a small peak located at 31.4°. This small peak has been discussed to be due to the presence of srilankite-like TiO_2 (JCPDS 21-1236).[52,63–65] We hypothesize that the appearance of srilankite TiO_2 may be due to the incorporation of triazine compounds into the titanate structure during nanowire growth as a result of the presence of melamine (which was employed as an *in situ* source of NH_4^+).[52,63–65] As the glass particle substrate created a large background signal, nanowire samples were also grown from fluorine-doped tin oxide (FTO) coated glass slides in order to provide a more detailed XRD pattern for reference (shown in Fig. 7a).

Nanorod-rod deposited particles were produced in a HTV employing growth conditions corresponding to HTV-18 (Table S1†). Fig. 7b shows that the TiO_2-composite seed particles were primarily anatase. Minor rutile content was observed due to the P25 particles incorporated into the film. It can be seen in Fig. 7b that, following hydrothermal treatment, the particle surface is covered with rutile (JCPDS 21-1276) nanorods. A small, sharp peak observed at 26.65° in Fig. 7 was indexed to SiO_2/quartz, presumably arising from the glass particle substrate, which may develop a crystalline content after multiple calcination steps at high temperatures.

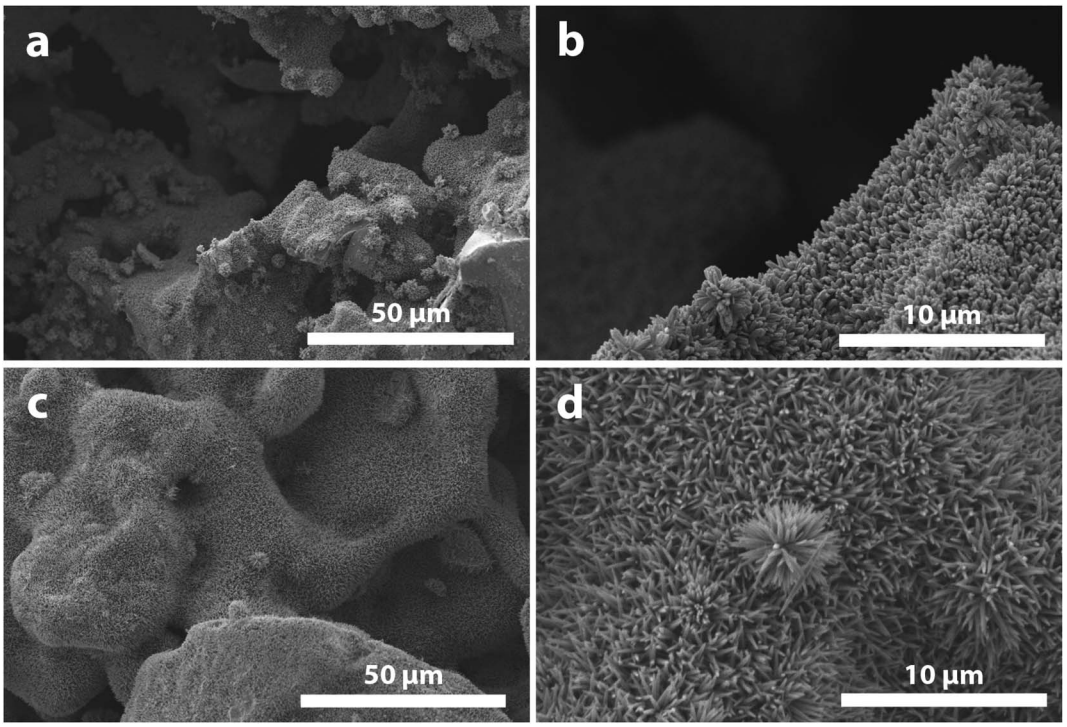

Fig. 5 Nanorod-deposited particles grown in (a and b) 1 : 1 HCl/H_2O solution with 12 mL of TTIP and (c and d) 3 : 1 HCl/H_2O solution with 20 mL of TTIP (corresponding to HTV-14 and HTV-18 in Table S1,† respectively).

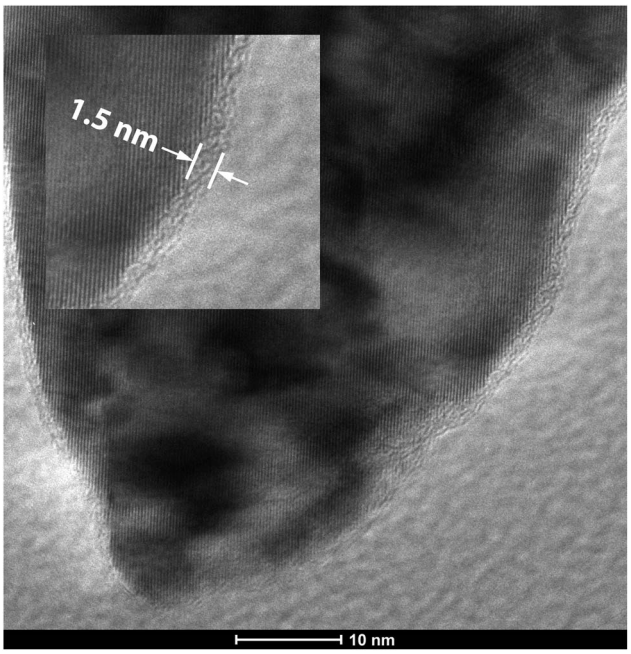

Fig. 6 TEM image of graphitic contamination layer of nanorod surface.

TEM imaging revealed that the nanorods consist of narrow nanorods (~50–60 nm diameter) that have fused together *via* their vertical faces (Fig. 8a). Lattice fringes with interplanar spacing of 2.9 Å and 3.2 Å (Fig. 8b) correspond with those of the rutile (110) and (001) planes, respectively. As the [110] axis is perpendicular to the vertical sides of the nanorods, it can be concluded that the nanorods grow with their [001] axis normal to the surface of the porous particles. The select-area electron diffraction (SAED) pattern (Fig. 8c) indicates that the nanorods are largely single crystalline throughout their length.

The band gap energies and absorbance of the CBD nanowire- and HTV nanorod-deposited particles were determined from the diffuse reflectance spectra. The nanowire- and nanorod-deposited particles were found to have band gap energies of 3.25 eV and 2.95 eV (Fig. 9a), respectively, which are in close agreement with band gap values reported for anatase and rutile TiO_2 in literature.[66–68] It can be seen in Fig. 9b that the optical absorption onset for the $TiCl_4$-treated seed particles is similar to that of rutile TiO_2, indicating that the $TiCl_4$ treatment yields rutile crystallites on the porous glass particle surface which act as nucleation sites for nanowire growth. It can therefore be concluded that the phase of the TiO_2 seed layer on porous particles does not affect the product phase of the nanowires or nanorods.

The anatase nanowire-deposited particles were measured to have a skeletal density of 2460 kg m^{-3} while the rutile nanorod-deposited particles have a skeletal density of 2540 kg m^{-3}, thus yielding effective densities of 1700 and 1790 kg m^{-3}, respectively, when the particles are fluidized in a 2.2 M aqueous Na_2CO_3 solution (~1200 kg m^{-3}) for water splitting. The nanowire- and nanorod-deposited particles were measured to have dry packed bed densities of 570 kg m^{-3} and 620 kg m^{-3}, respectively, each having a voidage of 0.42. These physical

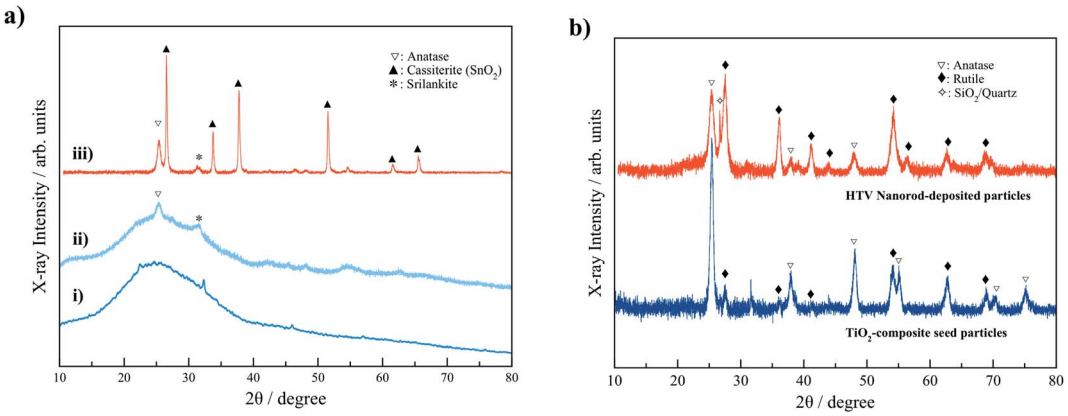

Fig. 7 (a) X-ray diffraction patterns of (i) TiCl4-treated seed particles, (ii) nanowire-deposited particles *via* CDB method and (iii) nanowires grown on FTO glass slides *via* CBD method. (b) X-ray diffraction patterns of the TiO_2-composite seed particles and the nanorod-deposited particles *via* HTV method.

characteristics place both particle types in Geldart class D (spoutable),[69] and yieldestimated minimum fluidization velocities of 0.0038 m s^{-1} (~0.32 L min^{-1}) and 0.0044 m s^{-1} (~0.37 L min^{-1}), respectively.

The low bulk particle densities and reduced fluidization velocities observed for both the nanowire- and nanorod-deposited particles yield several desirable and beneficial effects. The low bulk particle densities reduce the mass and, therefore, the momentum of individual particles, which, in turn, reduces the force of impact in particle-to-particle and particle-to-wall collisions. These reduced forces can serve to minimize any damage sustained during impact and significantly reduce the rate of attrition. Similarly, the low fluidization velocities typically provide gentler fluidization conditions and slower particle velocities, which helps to further reduce the rate of attrition. Finally, the low fluidization velocities also serve to reduce the total recirculation rate of the liquid phase. This, in turn, minimizes the energy required for pumping (thereby improving the overall energy efficiency of the process) and minimizes the capital cost of equipment as a smaller pump can be employed.

3.4. Attrition resistance

The large surface pores of the glass particles employed in this work create networks of "valley"- and "dimple"-like indentations surrounded by "peaks" and other large features (Fig. 10). These deep indentations provided large areas in which the mechanically weak TiO_2 photocatalyst coating could reside and remain protected from mechanical ablation during fluidization. Similarly, the outermost peaks served to minimize the contact area in particle-to-particle and particle-to-wall collisions, as well as to bear the force of impact. These effects are clearly

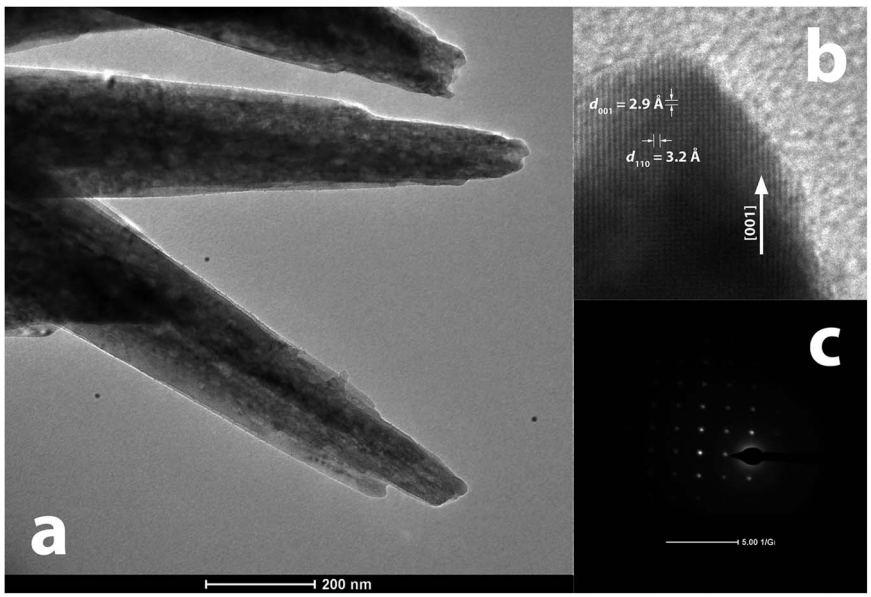

Fig. 8 TEM images of (a) hydrothermally grown nanorods and (b) the lattice fringes. (c) The SAED pattern for the nanorod shown in (b).

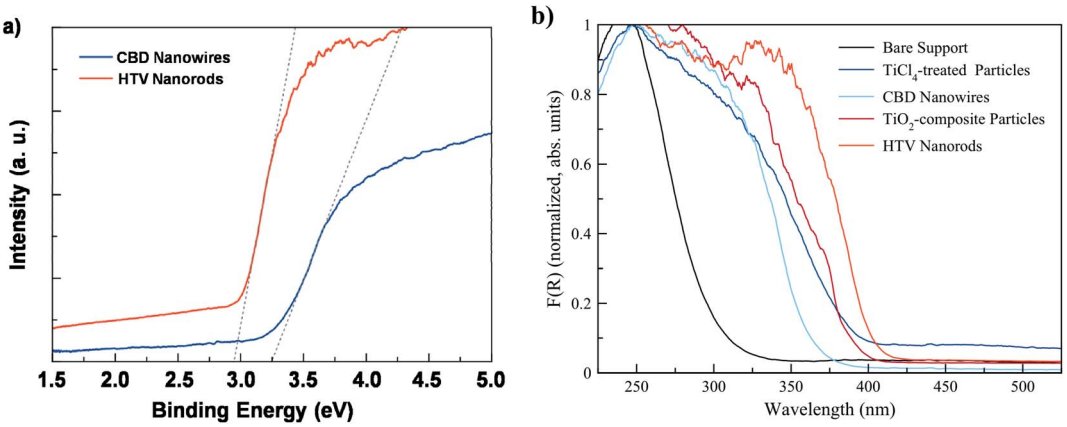

Fig. 9 (a) Tauc plots for the nanowire- and nanorod-deposited particles and (b) UV-Vis diffuse reflectance absorption spectra for bare, seeded and nanowire-/nanorod-deposited particles.

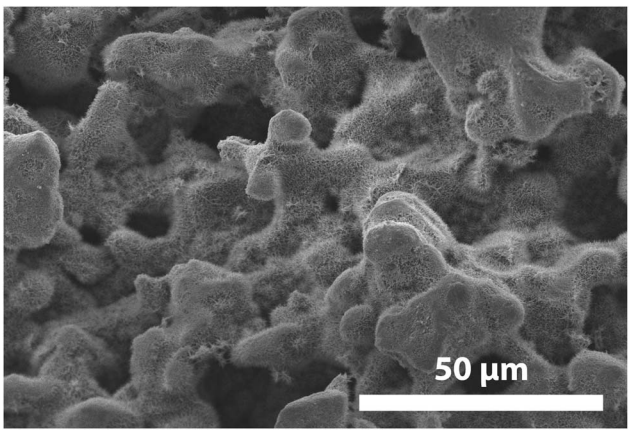

Fig. 10 SEM image of an anatase nanowire-deposited particle after 40 hours of fluidization. Nanowires were grown on the porous particles using a $[M_{cat}]/[V_{sol}]$ ratio of 0.025 g mL^{-1}.

demonstrated in Fig. 10, which shows an anatase nanowire-deposited photocatalyst particle that was fluidized for 40 hours. As seen in Fig. 10, the nanowires on the outermost points were compressed into a flat film or ablated from the particle surface (leaving a small bare area) due to collisions with other particles or the reactor wall, yet the nanowires residing in the deep indentations on the surface remain entirely intact. The small, damaged regions observed at the outermost points represent only a small portion of the visible nanostructure-deposited surface and are only observed under moderate-to-high magnification of select areas (thus making visual estimates of active surface area lost to mechanical attrition challenging).

To determine the attrition resistance of the porous glass design, a measured amount of nanorod-deposited particles (70 mL/42.82 g) and solid TiO_2-composite spheres (70 mL/81.32 g) (which were developed previously[51]) were individually placed the fluidized bed. The particles were fluidized in the reactor (no UV illumination) using deionized water to an expanded bed height of 24 cm for over 40 hours and the concentration of ablated TiO_2 particles suspended in solution was monitored. It can be seen in Fig. 11 that both particle types exhibit a 'break-in' period with a high initial rate of attrition as loosely bound or weak features are ablated from the particle surface. After 3.5 hours, most weakly bound TiO_2 is removed from the surface of the nanorod-deposited porous particles, however, this process continues for up to 5.5 hours for the solid TiO_2-composite spheres. Following the initial break-in period, the TiO_2-composite spheres continue to erode at a constant 0.011 g L^{-1} h^{-1} while the rate of TiO_2 ablated from the nanorod-deposited particles decreases significantly to a low 0.0011 g L^{-1} h^{-1}. The amount of TiO_2 ablated from the nanorod-deposited particles after 46 hours of fluidization was estimated to less than 1% of the total mass of TiO_2 deposited on the porous particles.

3.5. Potential applications

One-dimensional nanostructures, such as nanowires and nanorods can play a significant role in enhancing the quantum

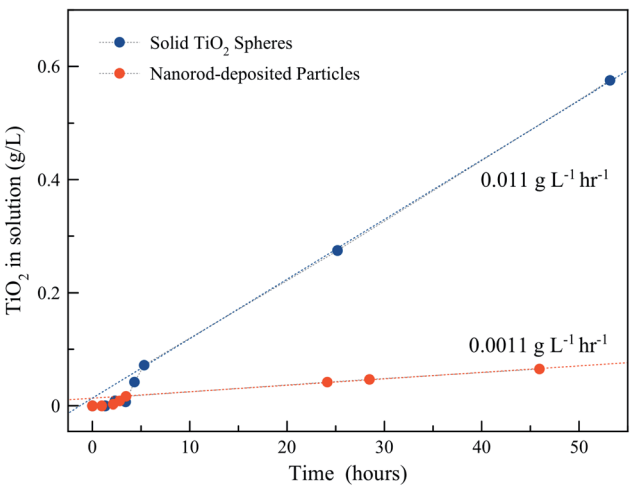

Fig. 11 Attrition resistance as determined by the concentration of ablated TiO_2 in solution (g per TiO_2 per L) for TiO_2 solid spheres (•) and nanorod-deposited particles on porous glass (•).

efficiencies of the photocatalytic systems, due to their peculiar characteristics, compared to those of their bulk counterparts. To name a few, one-dimensional nanostructures provide superior charge carrier separation, greater active surface area, and enhanced radiation utilization, compared to those typically observed for bulk photocatalyst materials. However, the conventional systems that can effectively utilize one-dimensional nanostructures face mass transfer limitation, in which the reactants inside the electrolyte cannot effectively interact with photocatalyst semiconductor.

It is known that fluidized bed reactors are designed to maintain high rate of mass transfer, so being an ideal candidate for thin film photocatalytic systems. However, fluidization of one-dimensional photocatalysts possess a considerable durability issues, due to particle–particle attrition. To maintain the structure of synthesized nanowires and nanorods, studies have proposed that the one-dimensional nanostructures can be deposition, or directly grown inside a porous substrate, in which remained challenging so far. The methodology proposed in this article can be consistently applied for reliable growth of anatase and rutile TiO_2 nanowires and nanorods, with controlled crystallography and morphology, inside the pores of glass substrates. The resulting coated photocatalytic system can have wide range of applications, including photodegradation of chemical contaminates and photoconversion of organics and water to value-added chemicals such as hydrogen, methane, and alcohols.

4. Conclusions

In this study, two separate methods have been developed that allow the large-scale fabrication of fluidizable nanowire and nanorod photocatalysts. Anatase TiO_2 nanowires were grown onto porous particles using a chemical bath deposition (CDB) process. The structural, elemental, and optical characteristics of the synthesized nanowires were studied through material characterization methods. For $[M_{cat}]/[M_{sol}] = 0.025\ g_{cat}\ mL^{-1}$, nanowires 53 nm × 2 μm long were reliably produced in batches sizes up to 30 g of the porous particles. Batch sizes were varied by using the appropriate volume of growth solution for the desire amount of porous glass particles. The nanowires were observed to grow in high density over the entire particle surface for all conditions studied.

Rutile TiO_2 nanorods were produced using a modified hydrothermal method in batches up to 25 g of particles. The quality of the resulting nanorod films was observed to vary according to the initial reactor conditions. A growth quality factor, R_q, was defined that allowed for the careful calculation of the hydrothermal reactor conditions necessary to tailor the morphology of the synthesized film. R_q allowed for good quality films to be grown on varying different batch amounts and even different hydrothermal reactor sizes. For an initial growth solution having 150 mL of HCl/50 mL of H_2O/20 mL of TTIP, high-density nanorod films of 2.8 μm thick could be obtained. Interestingly, it was found that the porous glass beads were highly effective in reducing the rate of photocatalyst attrition. The protective features of the particles reduced the rate of attrition by 10× to near negligible levels, enabling the development of highly efficient photocatalytic systems for wide spectrum of applications, including water splitting and decontamination of organic pollutants in water.

Conflicts of interest

There are no conflicts to declare.

Acknowledgements

The authors would like to thank the Natural Sciences and Engineering Research Council (NSERC) of Canada for their sponsorship and contributions, the Bioimaging Laboratory at the University of British Columbia (UBC) for their assistance with SEM and TEM imaging.

References

1 V. H. Nguyen, *et al.*, Novel p−n heterojunction nanocomposite: TiO2 Qds/ZnBi2O4 photocatalyst with considerably enhanced photocatalytic activity under visible-light irradiation, *J. Phys. Chem. C*, 2020, **124**, 27519–27528.
2 K. E. Karakitsou and X. E. Verykios, Influence of catalyst parameters and operational variables on the photocatalytic cleavage of water, *J. Catal.*, 1992, **134**, 629–634.
3 K. E. Karakitsou and X. E. Verykios, Definition of the Intrinsic Rate of Photocatalytic Cleavage of Water Over Pt-RuO2/TiO2 Catalysts, *J. Catal.*, 1995, **152**, 360–367.
4 H. Muraki, T. Saji, M. Fujihira and S. Aoyagui, Photocatalytic oxidation of water to hydrogen peroxide by irradiation of aqueous suspensions of TiO2, *J. Electroanal. Chem. Interfacial Electrochem.*, 1984, **169**, 319–323.
5 K. Reilly, B. Fang, F. Taghipour and D. P. Wilkinson, Enhanced photocatalytic hydrogen production in a UV-irradiated fluidized bed reactor, *J. Catal.*, 2017, **353**, 63–73.
6 J. Jitputti, Y. Suzuki and S. Yoshikawa, Synthesis of TiO2 nanowires and their photocatalytic activity for hydrogen evolution, *Catal. Commun.*, 2008, **9**, 1265–1271.
7 G. Wang, *et al.*, Hydrogen-treated TiO2 nanowire arrays for photoelectrochemical water splitting, *Nano Lett.*, 2011, **11**, 3026–3033.
8 H. J. Yun, H. Lee, J. B. Joo, N. D. Kim and J. Yi, Effect of TiO2 Nanoparticle Shape on Hydrogen Evolution via Water Splitting, *J. Nanosci. Nanotechnol.*, 2011, **11**, 1688–1691.
9 S. Chuangchote, J. Jitputti, T. Sagawa and S. Yoshikawa, Photocatalytic activity for hydrogen evolution of electrospun TiO2 nanofibers, *ACS Appl. Mater. Interfaces*, 2009, **1**, 1140–1143.
10 J.-M. Wu, *et al.*, Large-scale preparation of ordered titania nanorods with enhanced photocatalytic activity, *Langmuir*, 2005, **21**, 6995–7002.
11 B. Li, J.-M. Wu, T.-T. Guo, M.-Z. Tang and W. Wen, A facile solution route to deposit TiO2 nanowire arrays on arbitrary substrates, *Nanoscale*, 2014, **6**, 3046–3050.

12 X. Wang, Z. Li, J. Shi and Y. Yu, One-Dimensional Titanium Dioxide Nanomaterials: Nanowires, Nanorods, and Nanobelts, *Chem. Rev.*, 2014, **114**, 9346–9384.
13 Z. Yang, *et al.*, Factors influencing the photocatalytic activity of rutile TiO2 nanorods with different aspect ratios for dye degradation and Cr(vi) photoreduction, *Phys. Chem. Chem. Phys.*, 2015, **17**, 18670–18676.
14 K. Shankar, *et al.*, Recent Advances in the Use of TiO 2 Nanotube and Nanowire Arrays for Oxidative Photoelectrochemistry, *J. Phys. Chem. C*, 2009, **113**, 6327–6359.
15 J. Cai, *et al.*, Self-cleaning, broadband and quasi-omnidirectional antireflective structures based on mesocrystalline rutile TiO2 nanorod arrays, *Energy Environ. Sci.*, 2012, **5**, 7575.
16 A. Jaggessar, *et al.*, Mechanical, bactericidal and osteogenic behaviours of hydrothermally synthesised TiO 2 nanowire arrays, *J. Mech. Behav. Biomed. Mater.*, 2018, **80**, 311–319.
17 T. Kanki, S. Hamasaki, N. Sano, A. Toyoda and K. Hirano, Water purification in a fluidized bed photocatalytic reactor using TiO2-coated ceramic particles, *Chem. Eng. J.*, 2005, **108**, 155–160.
18 A. Bhargava, M. F. Kabir, E. Vaisman, C. H. Langford and A. Kantzas, Novel Technique to Characterize the Hydrodynamics and Analyze the Performance of a Fluidized-Bed Photocatalytic Reactor for Wastewater Treatment, *Ind. Eng. Chem. Res.*, 2004, **43**, 980–989.
19 F. Haque, E. Vaisman, C. H. Langford and A. Kantzas, Preparation and performance of integrated photocatalyst adsorbent (IPCA) employed to degrade model organic compounds in synthetic wastewater, *J. Photochem. Photobiol., A*, 2005, **169**, 21–27.
20 M. F. Kabir, E. Vaisman, C. H. Langford and A. Kantzas, Effects of hydrogen peroxide in a fluidized bed photocatalytic reactor for wastewater purification, *Chem. Eng. J.*, 2006, **118**, 207–212.
21 E. Vaisman, M. F. Kabir, a. Kantzas and C. H. Langford, A fluidized bed photoreactor exploiting a supported photocatalyst with adsorption pre-concentration capacity, *J. Appl. Electrochem.*, 2005, **35**, 675–681.
22 M. F. Kabir, F. Haque, E. Vaisman, C. H. Langford and A. Kantzas, Disinfecting E.coli Bacteria In Drinking Water Using A Novel Fluidized Bed Reactor, *Int. J. Chem. React. Eng.*, 2003, **1**(1), DOI: 10.2202/1542-6580.1101.
23 A. N. Banerjee, The design, fabrication, and photocatalytic utility of nanostructured semiconductors: focus on TiO2-based nanostructures, *Nanotechnol., Sci. Appl.*, 2011, **4**, 35–65.
24 N. Bao, X. Feng and C. Grimes, a. Self-organized one-dimensional TiO 2 nanotube/nanowire array films for use in excitonic solar cells: A review, *J. Nanotechnol.*, 2012, **2012**, 645931.
25 B. Liu, J. E. Boercker and E. S. Aydil, Oriented single crystalline titanium dioxide nanowires, *Nanotechnology*, 2008, **19**, 505604.
26 Y. Li, M. Guo, M. Zhang and X. Wang, Hydrothermal synthesis and characterization of TiO2 nanorod arrays on glass substrates, *Mater. Res. Bull.*, 2009, **44**, 1232–1237.
27 Y. Li, M. Zhang, M. Guo and X. Wang, Hydrothermal growth of well-aligned TiO2 nanorod arrays: Dependence of morphology upon hydrothermal reaction conditions, *Rare Met.*, 2010, **29**, 286–291.
28 I. S. Cho, *et al.*, Branched TiO_2 nanorods for photoelectrochemical hydrogen production, *Nano Lett.*, 2011, **11**, 4978–4984.
29 Z. Wei, Y. Yao, T. Huang and A. Yu, Solvothermal growth of well-aligned TiO2 nanowire arrays for dye-sensitized solar cell: Dependence of morphology and vertical orientation upon substrate pretreatment, *Int. J. Electrochem. Sci.*, 2011, **6**, 1871–1879.
30 W.-Q. Wu, *et al.*, Hydrothermal fabrication of hierarchically anatase TiO2 nanowire arrays on FTO glass for dye-sensitized solar cells, *Sci. Rep.*, 2013, **3**, 1352.
31 W.-Q. Wu, *et al.*, Hierarchical oriented anatase TiO2 nanostructure arrays on flexible substrate for efficient dye-sensitized solar cells, *Sci. Rep.*, 2013, **3**, 1892.
32 W.-Q. Wu, Y.-F. Xu, C.-Y. Su and D.-B. Kuang, Ultra-long anatase TiO 2 nanowire arrays with multi-layered configuration on FTO glass for high-efficiency dye-sensitized solar cells, *Energy Environ. Sci.*, 2014, **7**, 644–649.
33 W.-Q. Wu, *et al.*, A family of vertically aligned nanowires with smooth, hierarchical and hyperbranched architectures for efficient energy conversion, *Nano Energy*, 2014, **9**, 15–24.
34 L. Chu, *et al.*, A general method for preparing anatase TiO_2 treelike-nanoarrays on various metal wires for fiber dye-sensitized solar cells, *Sci. Rep.*, 2014, **4**, 4420.
35 D.-D. Qin, *et al.*, Hydrothermal Growth and Photoelectrochemistry of Highly Oriented, Crystalline Anatase TiO 2 Nanorods on Transparent Conducting Electrodes, *Chem. Mater.*, 2015, **27**(12), 4180–4183.
36 T. Peng, S. Ray, S. S. Veeravalli, J. A. Lalman and F. Arefi-Khonsari, The role of hydrothermal conditions in determining 1D TiO2 nanomaterials bandgap energies and crystal phases, *Mater. Res. Bull.*, 2018, **105**, 104–113.
37 N. Kitazawa and M. Aono, Growth and photo-electrochemical properties of rutile TiO 2 nanowire arrays prepared by the hydrothermal method, *Int. J. Mater. Res.*, 2019, **110**, 268–274.
38 B. Liu and E. S. Aydil, Growth of oriented single-crystalline rutile TiO 2 nanorods on transparent conducting substrates for dye-sensitized solar cells, *J. Am. Chem. Soc.*, 2009, **131**, 3985–3990.
39 K. E. Karakitsou and X. E. Verykios, Effects of altervalent cation doping of titania on its performance as a photocatalyst for water cleavage, *J. Phys. Chem.*, 1993, **97**, 1184–1189.
40 Z. Ding, G. Q. Lu and P. F. Greenfield, Role of the Crystallite Phase of TiO 2 in Heterogeneous Photocatalysis for Phenol Oxidation in Water, *J. Phys. Chem. B*, 2000, **104**, 4815–4820.
41 T. Sreethawong, Y. Suzuki and S. Yoshikawa, Synthesis, characterization, and photocatalytic activity for hydrogen evolution of nanocrystalline mesoporous titania prepared

by surfactant-assisted templating sol–gel process, *J. Solid State Chem.*, 2005, **178**, 329–338.

42 J. Jitputti, S. Pavasupree, Y. Suzuki and S. Yoshikawa, Synthesis and photocatalytic activity for water-splitting reaction of nanocrystalline mesoporous titania prepared by hydrothermal method, *J. Solid State Chem.*, 2007, **180**, 1743–1749.

43 X. Chen, S. Shen, L. Guo and S. S. Mao, Semiconductor-based photocatalytic hydrogen generation, *Chem. Rev.*, 2010, **110**, 6503–6570.

44 D. Y. C. Leung, *et al.*, Hydrogen production over titania-based photocatalysts, *ChemSusChem*, 2010, **3**, 681–694.

45 T. Luttrell, *et al.*, Why is anatase a better photocatalyst than rutile?–Model studies on epitaxial TiO2 films, *Sci. Rep.*, 2014, **4**, 4043.

46 H. Li, *et al.*, Titanate nanowire as a precursor for facile morphology control of TiO2catalysts with enhanced photocatalytic activity, *J. Alloys Compd.*, 2016, **687**, 927–936.

47 S. M. Lee, *et al.*, Morphology control in anatase TiO2 mesocrystals through hydrofluoride incorporation for photocatalytic application, *J. Nanosci. Nanotechnol.*, 2016, **16**, 10592–10596.

48 S. P. Hong, *et al.*, Comprehensive Study on the Morphology Control of TiO2 Nanorods on Foreign Substrates by the Hydrothermal Method, *Cryst. Growth Des.*, 2018, **18**, 6504–6512.

49 Y. Guo, G. Liu, Z. Ren, A. Piyadasa and P.-X. Gao, Single crystalline brookite titanium dioxide nanorod arrays rooted on ceramic monoliths: a hybrid nanocatalyst support with ultra-high surface area and thermal stability, *CrystEngComm*, 2013, **15**, 8345.

50 X. Cai, *et al.*, Dye-sensitized solar cells with vertically aligned TiO2 nanowire arrays grown on carbon fibers, *ChemSusChem*, 2014, **7**, 474–482.

51 B. Fang, *et al.*, Large-scale synthesis of TiO2microspheres with hierarchical nanostructure for highly efficient photodriven reduction of CO2to CH4, *ACS Appl. Mater. Interfaces*, 2014, **6**, 15488–15498.

52 J. Sun, W. Wen and J.-M. Wu, Low-temperature transformation of titania thin films from amorphous nanowires to crystallized nanoflowers for heterogeneous photocatalysis, *J. Am. Ceram. Soc.*, 2013, **96**, 2109–2116.

53 J.-M. Wu and J.-X. Yin, A facile solution-based approach to a photocatalytic active branched one-dimensional TiO 2 array, *RSC Adv.*, 2015, **5**, 3465–3469.

54 L. A. Al-Hajji, *et al.*, Impact of calcination of hydrothermally synthesized TiO2 nanowires on their photocatalytic efficiency, *J. Mol. Struct.*, 2020, **1200**, 127153.

55 M. Keshmiri, M. Mohseni and T. Troczynski, Development of novel TiO2 sol–gel-derived composite and its photocatalytic activities for trichloroethylene oxidation, *Appl. Catal. B Environ.*, 2004, **53**, 209–219.

56 N. Jackson and C. Wang, Attachment of TiO2 Powders to Hollow Glass Microbeads: Activity of the TiO2-Coated Beads in the Photoassisted Oxidation of Ethanol to Acetaldehyde, *J. Electrochem. Soc.*, 1991, **138**, 3660–3664.

57 Y. Chang, *et al.*, Effect of post-heat treatment on the photocatalytic activity of titanium dioxide nanowire membranes deposited on a Ti substrate, *RSC Adv.*, 2017, **7**, 21422–21429.

58 A. a. Vega, M. Keshmiri and M. Mohseni, Composite template-free TiO2 photocatalyst: Synthesis, characteristics and photocatalytic activity, *Appl. Catal. B Environ.*, 2011, **104**, 127–135.

59 M. Rajabi, S. Shogh and A. Iraji zad, Defect study of TiO2 nanorods grown by a hydrothermal method through photoluminescence spectroscopy, *J. Lumin.*, 2015, **157**, 235–242.

60 S. Shanmugam, A. Gabashvili, D. S. Jacob, J. C. Yu and A. Gedanken, Synthesis and Characterization of TiO 2 @C Core−Shell Composite Nanoparticles and Evaluation of Their Photocatalytic Activities, *Chem. Mater.*, 2006, **18**, 2275–2282.

61 L. W. Zhang, H. B. Fu and Y. F. Zhu, Efficient TiO2 photocatalysts from surface hybridization of TiO2 particles with graphite-like carbon, *Adv. Funct. Mater.*, 2008, **18**, 2180–2189.

62 J. Zhong, F. Chen and J. Zhang, Carbon-Deposited TiO 2 : Synthesis, Characterization, and Visible Photocatalytic Performance, *J. Phys. Chem. C*, 2010, **114**, 933–939.

63 J.-M. Wu and H. X. Xue, Photocatalytic active titania nanowire arrays on Ti substrates, *J. Am. Ceram. Soc.*, 2009, **92**, 2139–2143.

64 L.-L. Lai, L.-L. Huang and J.-M. Wu, K2TiO(C2O4)2 -mediated synthesis of rutile TiO2 mesocrystals and their ability to assist photodegradation of sulfosalicylic acid in water, *RSC Adv.*, 2014, **4**, 49280–49286.

65 L.-L. Lai and J.-M. Wu, A facile synthesis of hierarchical TiO 2 for dye adsorption and photocatalysis, *RSC Adv.*, 2014, **4**, 36212.

66 K. Madhusudan Reddy, S. V. Manorama and A. Ramachandra Reddy, Bandgap studies on anatase titanium dioxide nanoparticles, *Mater. Chem. Phys.*, 2002, **78**, 239–245.

67 D. Reyes-Coronado, *et al.*, Phase-pure TiO(2) nanoparticles: anatase, brookite and rutile, *Nanotechnology*, 2008, **19**, 145605.

68 D. O. Scanlon, *et al.*, Band alignment of rutile and anatase TiO_2, *Nat. Mater.*, 2013, **12**, 798–801.

69 D. Geldart, Types of gas fluidization, *Powder Technol.*, 1973, **7**, 285–292.